Available online at www.sciencedirect.com

jmr&t Journal of Materials Research and Technology

journal homepage: www.elsevier.com/locate/jmrt

Original Article

Effect of solution treatment on microstructure and stress rupture properties of precipitation hardened IN718 superalloy fabricated by laser powder-bed fusion process

A.M. Chizari [a,b], A. Kermanpur [a,*], E. Foroozmehr [c], A. Rezaeian [a], F. Sadeghi [d], Ali Rezaei [b]

[a] Department of Materials Engineering, Isfahan University of Technology, Isfahan, 84156-83111, Iran
[b] Noura Co., Isfahan Science and Technology Town, Iran
[c] Department of Mechanical Engineering, Isfahan University of Technology, Isfahan, 84156-83111, Iran
[d] Graduate Institute of Ferrous and Energy Materials Technology, Pohang University of Science and Technology, Pohang, 37673, Republic of Korea

ARTICLE INFO

Article history:
Received 27 August 2022
Accepted 12 October 2022
Available online 17 October 2022

Keywords:
Laser powder-bed fusion
IN718 superalloy
Precipitation hardening
Stress rupture properties
Microstructure

ABSTRACT

Effect of solution temperature in precipitation hardening on microstructure and stress rupture properties of IN718 superalloy fabricated by laser powder-bed fusion (LPBF) process is investigated. The LPBF samples were solution treated at 980, 1060 and 1130 °C, followed by two-step aging at 720 and 620 °C, each for 8 h. The results showed that the solution treatment at 980 °C was not suitable for stress rupture properties due to the formation of δ and Laves phases along grain boundaries, which promoted intergranular fracture. On the other hand, non-uniform grain growth occurred in the sample solution treated at 1130 °C, which reduced stress rupture properties. The solution treatment at 1060 °C was found more suitable to improve stress rupture behavior of the LPBF IN718 superalloy at 650 °C. The rupture life of the alloy approached 87 h due to the formation of suitable grain structure and distribution of γ′/γ″ strengthening phases.

1. Introduction

Inconel 718 (IN718) is one of the nickel-based superalloys which has been widely used in aeronautical and petrochemical industries due to its excellent mechanical performance and high corrosion resistance at elevated temperatures [1–3]. This age-hardenable superalloy is mainly produced by common methods such as forging and casting [4]. However, because of the high waste of raw materials and the long manufacturing process, these production methods brings huge economic costs for manufacturers. On the other hand, in some cases, the complexity of the parts in terms of geometric

* Corresponding author.
E-mail address: ahmad_k@iut.ac.ir (A. Kermanpur).
https://doi.org/10.1016/j.jmrt.2022.10.047

shape makes it impossible to produce them with conventional methods or leads to an expensive, timely procedure. In recent years, additive manufacturing (AM) techniques have been emerged which have not only reduced the limitations of the conventional manufacturing processes, but also have many benefits. Laser powder-bed fusion (LPBF) is one of the common metal AM techniques which makes possibilities to fabricate near-net-shape metal parts with complex structures [5,6]. In addition, reducing the number of manufacturing steps in the LPBF process, leads to saving times and energy consumption. Nevertheless, due to some inherent features of the LPBF process, such as high thermal gradient and rapid solidification rate, large amounts of residual stresses are formed in the as-built parts. Moreover, the rapid solidification rate leads to microsegregation of the alloying components and the establishment of non-equilibrium phases, which is related to the growth of dendrites containing segregated alloying elements. Thus, suitable heat treatments are needed to adjust the microstructure of IN718 components for completion of recrystallization, dissolution of primary dendrites, uniform distribution of alloying elements in the matrix, and precipitation of strengthening γ' and γ'' phases.

Many researchers have been conducted so far to investigate the effects of heat treatment on the microstructure and mechanical properties of the LPBF fabricated IN718 parts [7–9]. Overall, the results of these studies showed that heat treatment could dissolve primary dendrites in the microstructure and make a uniform distribution of alloying elements in the matrix. As a result, by performing heat treatment, the yield and tensile strength of the samples improved, but their elongation reduced compared to the as-built components [8,10]. Probstle et al. [11] examined the creep performances of LPBFed IN718 compared with conventionally cast and wrought alloys. Their results showed that the creep life of the LPBF specimens was longer than the conventional samples due to the higher amount of strengthening precipitates and the lack of δ phases. The creep performances of the LPBF fabricated IN718 in different building directions (BDs), which was studied by Kuo et al. [12], showed that the sample produced in horizontal direction (related to BD) exhibited a shorter creep life than the vertical direction specimen. Shi et al. [13] were also studied the creep behavior of IN718 alloy fabricated by LPBF, which was heat-treated under different conditions. The creep results revealed that the homogenized sample (HA) experienced longer creep life than the solution sample (SA), which was attributed to higher dislocation density within grains in the HA specimen. However, this research has not investigated the effect of annealing at higher temperatures than the homogenization treatment on stress–rupture properties.

Since IN718 is an age-hardenable, high temperature material, heat treatment has a significant effect on the properties of this alloy, especially stress-rupture behavior. According to the author's knowledge, the number of researches conducted on the effect of heat treatment on stress–rupture properties of the LPBF fabricated IN718 is limited. Many aspects of creep mechanisms have not been adequately studied so far. This study aims to study the effect of solution temperature on microstructure, stress rupture properties, and failure mechanism of the LPBFed IN718 alloy. The stress rupture properties of the alloys at 650 °C/750 MPa is investigated based on microstructural analysis, and the governing creep mechanism is discussed.

2. Materials and experimental procedures

Fig. 1 represents the commercial pre-alloyed IN718 superalloy powder with a size range from 15 to 60 μm used in the present work. The chemical composition of the alloy powder is listed in Table 1. As given in Table 2, the samples were built with optimized process parameters by the Noura M100P machine. Stress-rupture samples were built with the size of $11 \times 43 \times 11$ mm^3 as illustrated in Fig. 2(a). The LPBF process was done under protective argon gas to minimize oxidation during manufacturing. After the LPBF process, the as-built specimens were heat-treated to different cycles of solution treatment at 980 °C, 1060 °C, and 1130 °C (1 h/air cooling), which were named as HT980, HT1060, and HT1130, respectively. The same double-stage aging procedure were applied to all samples, which includes one step at 720 °C for 8 h, furnace cool to 620 °C, and hold at 620 °C for 8 h. Microstructural of the heat-treated samples were characterized by SEM (Philips, XI30) and FE-SEM (FEI Quanta 450). The crystallographic texture was investigated by an electron backscatter diffraction detector (EBSD), and EDS (Oxford X-MaxN) was used to clarify the Chemical composition of components. The samples were initially abraded by SiC papers and then polished by 1 μm alumina suspension. Then Kallings solvable (40 ml HCl, 40 ml CH_3COOH, and 2 gr $CuCl_2$) was used for SEM examinations. TEM thin foil samples with 100 μm in thickness and 3 mm in diameter were prepared by jet-polishing in the mixed solution of 95% ethanol and 5% perchloric acid at −30 °C.The TEM and STEM-EDS data were interpretated by Gatan Digital Micrograph and Oxford Aztec software respectively. Stress rupture test samples were machined according to ASTM E139-M [14], as shown in Fig. 2(b). The stress rupture tests were conducted at 650 °C with a constant stress of 750 MPa using the Santam creep test machine. Moreover, to ensure the reproducibility of the stress-rupture results, it was repeated at least 2 times for each sample.

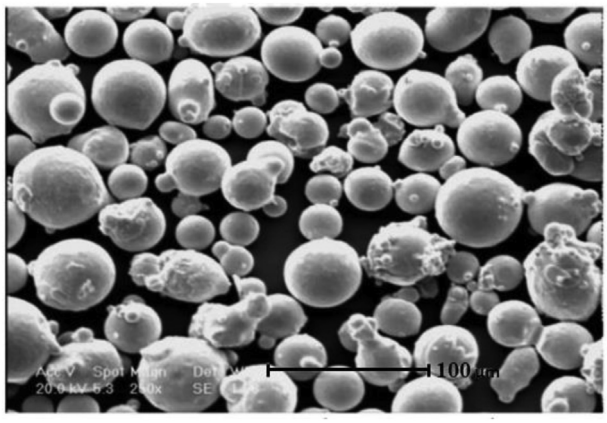

Fig. 1 – SEM micrograph of pre-alloyed IN718 powder.

Table 1 – Chemical composition of the IN718 Powder (wt %).

Element	Ni	Cr	Fe	Mo	Nb	Ti	Mn	AL	C
Content	54.39	17.57	Bal.	3.1	4.82	0.93	0.35	0.65	0.06

3. Results

3.1. *The as-built microstructure*

Fig. 3 displays the schematic view of laser scan strategy and the microstructures of the as-built specimen perpendicular to BD (Y-Z Plane). Fig. 3(a) shows that the specimens were fabricated by meander scanning strategy, which rotated 90° between the layers. In the optical micrograph of Fig. 3(b), molten pools are formed next to each other in typical arc-shaped form and layer by layer resulting from Gaussian energy distribution of the laser scan [16]. They were 30 μ m in thickness and 100 μ m in width, which are related to the spot diameter and layer thickness, respectively. The SEM images with higher magnification of the as-built microstructures are displayed in Fig. 3(c) and (d). Columnar grains as well as melt pools and interlayer boundaries are indicated. As can be seen, the cellular dendrites are formed very fine and grown differently in various regions. This indicates that the melt pool temperature gradient is complicated, although the overall heat flow direction is parallel to BD. Further details of cellular dendrites at a higher magnification (Fig. 3(d)) shows the Laves phase, formed by a chainlike morphology (indicated by an arrow) within the cell walls. The presence of Laves phase has also been reported in literature and is well-known to form in the as-built LPBF IN718 [5,15,17,18]. They need to be dissolved in the subsequent heat treatments.

3.2. *The heat-treated microstructures*

Fig. 4 shows the SEM micrographs and EDS analysis of the samples after heat treatments. As seen in Fig. 4(a and d), a large number of δ (Ni_3Nb) phase with short-rod and needle-like morphologies were formed in the matrix and grain boundaries of the HT980 sample (presented as EDS spots 1 and 2 in Fig. 4(d)). However, after the solution treatment at 1060 °C (Fig. 4(b and e)), the short-rod δ phases are entirely eliminated from the matrix, and the needle-like δ phase (EDS spot 3 in Fig. 4(e)) is reduced from grain boundaries. Moreover, EDS analysis and morphology of the particle 4 (EDS spot 4 in Fig. 4(e)) show that carbides with blocky-shaped, which included at grain boundaries in the HT1060 sample, as also reported in [19]. Regarding the high Nb content of particles 5 and 6 and also their morphology, they are supposed to be blocky (Nb, Ti) C carbides, which are distributed continuously in the microstructure of the HT 1130 sample. In fact, by performing the solution treatment at 1130 °C, most of the δ phases were dissolved into the matrix (as indicated in Fig. 4(c) and (f)). However, the carbides became coarser under this condition. With regards to the high Nb content of these particles, it could be resulted in unfavorable creep properties by limiting the formation of γ'' precipitates, as reported by McLouth et al. [20].

Fig. 5 displays the EBSD information of the heat-treated samples. In Fig. 5(a), the orientation map of the HT980 sample displays columnar grains along BD with high aspect ratios, and partial recrystallization in very small areas. The average grain diameter of the HT980 sample was measured as 13.7 μm, which is close to the as-built condition with 14.2 μm diameter. The pinning effect of the δ phases led to similar grain size and morphology in the as-built and HT980 specimens. However, with increasing solution temperature to 1060 °C (HT1060 sample), more recrystallization is occurred relative to the HT980 alloy (Fig. 5(b)). The formation of fine equiaxed grains in the microstructure has reduced the average grain size to 10.8 μm; however, columnar grains still remain at different regions of the HT1060 sample. Finally, complete recrystallization is occurred with solution treatment at 1130 °C (Fig. 5(c)). Due to grain growth under this condition, the average grain diameter is increased significantly and reached to about 27.4 μm.

On the other hand, the boundary maps shown in Fig. 5(d)-5(f) display relatively higher amounts of low-angle grain boundaries (LAGBs) in the HT980 and HT1060 samples compared to the HT1130 one. The fraction of the LAGBs for the HT980, HT1060, and HT1130 samples was measured as about 22%, 19%, and 6%, respectively. Furthermore, high-angle grain boundaries (HAGBs, marked by black lines) in the columnar grains of the HT980 and HT1060 samples show a serration morphology that will be discussed in the next section.

The pole figures (PFs) of the heat-treated samples are displayed in Fig. 5(j)-5(l). The strong <001> texture component that was also observed in the as-built condition, could be determined from the (001) PF in the HT980 specimen (Fig. 5(j)). With increasing solution temperature to 1060 °C, this texture component makes relatively weaker in HT1060 sample (Fig. 5(k)). Finally, the texture is entirely removed from the microstructure, and random orientations are formed in the HT1130 sample, as can be determined from the (001) PF (Fig. 5(l)).

Fig. 6 illustrates the kernel average misorientation (KAM) maps of the heat-treated samples. It is known that the KAM maps represent stress situations regarding the dislocation

Table 2 – LPBF process parameters used to fabricate IN718 samples in this study.

Laser Power (W)	Laser velocity (mm/s)	Layer thickness (μ m)	Volumetric energy density (J/mm^3)	Scanning strategy	Protective gas
150	1000	30	83	Meander	Ar

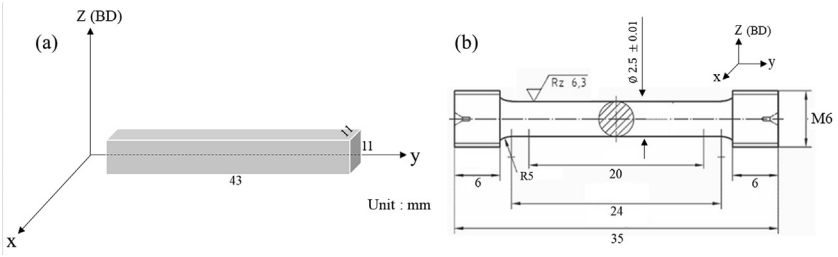

Fig. 2 – (a) Schematic diagram of the as-built cubic-shaped (BD: building direction) and (b) the geometry of the stress rupture test samples [15].

accumulations by calculating the misorientation angle of the neighboring points. In fact, increasing the misorientation angle between two points indicates a higher dislocation concentration. The distribution and density of dislocations has widely investigated through KAM maps by many researchers [13,21,22]. As shown in Fig. 6, the higher local misorientations in HT980 sample shows the existence of a high level of residual stresses, which is the result of the high dislocation density. By performing solution treatment at temperatures of 1060 °C (HT1060) and 1130 °C (HT1130) (Fig. 6(b) and (c)), the amount of misorientaions angle between the points is decreased, which is the result of reducing the dislocation density.

The influence of the solution temperature on substructures and phase formation including strengthing phases (γ″ and γ′) in the samples with different heat treatments was characterized by TEM investigations. STEM images of the HT980 and HT1060 samples related to EDS patterns are shown in Fig. 7. The chemical composition differences between matrix and precipitates are specified by EDS from the γ matrix (Spectrum 1). TEM-EDS analysis of the particles 3 and 4 regarding their morphology shows that they both might be needle-shaped δ phases that precipitated at grain boundaries in the HT980 and HT1060 samples, as seen in Fig. 4(d) and (e). The formation of the δ phase leads to the creation of Nb-free areas around these particles. The EDS analysis of spectrum 2 confirms this Nb depletion. Particles 5 and 6 with respect to their chemical composition and morphology are supposed to be nano-scale γ″ and γ′, respectively, formed inside the grains in the HT1060 sample. These precipitates are seen with the same features in the HT980 sample (Fig. 7(c)). As reported by many authors, the γ″ phases are formed in the microstructure of IN718 in both acicular (mostly in grain boundaries) and ellipsoidal (mainly inside the grains) morphologies [23,24]. The acicular γ″ phase is very similar in size, morphology, and also chemical composition to the acicular δ phase [23]. Therefore, EDS analysis is insufficient to separate these two precipitates from each other and can only be identified by using selected area electron diffraction (SAED) patterns.

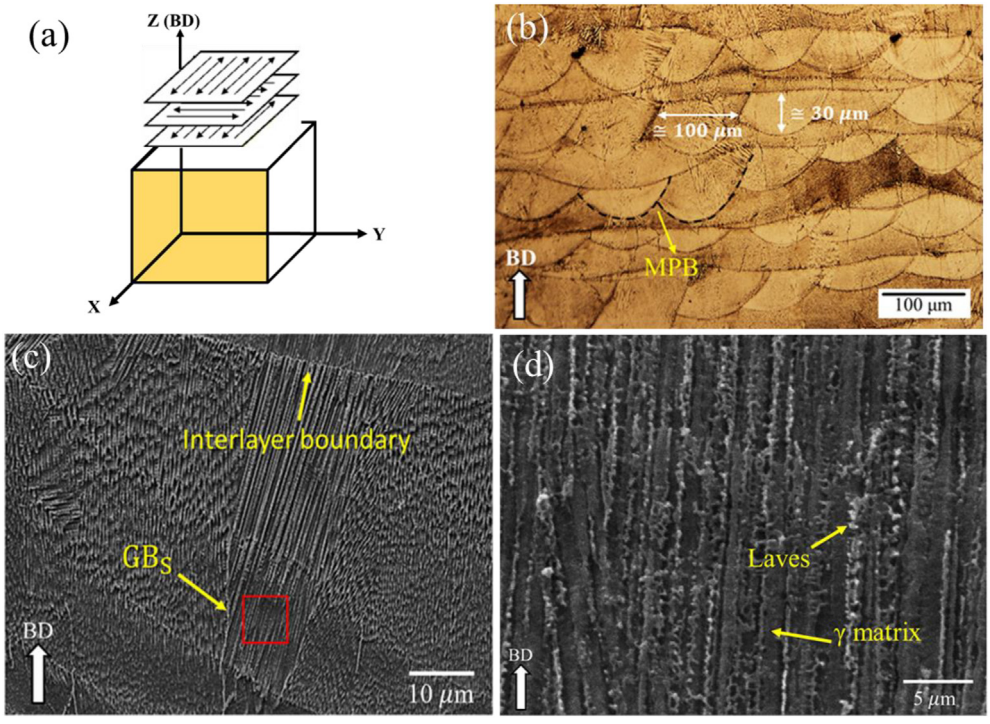

Fig. 3 – (a) Schematic illustration of layers scanning strategies, (b) optical and (c, d) SEM micrographs of the as-built IN718 alloy at different magnifications from Y-Z plane, showing molten pools and dendritic structure.

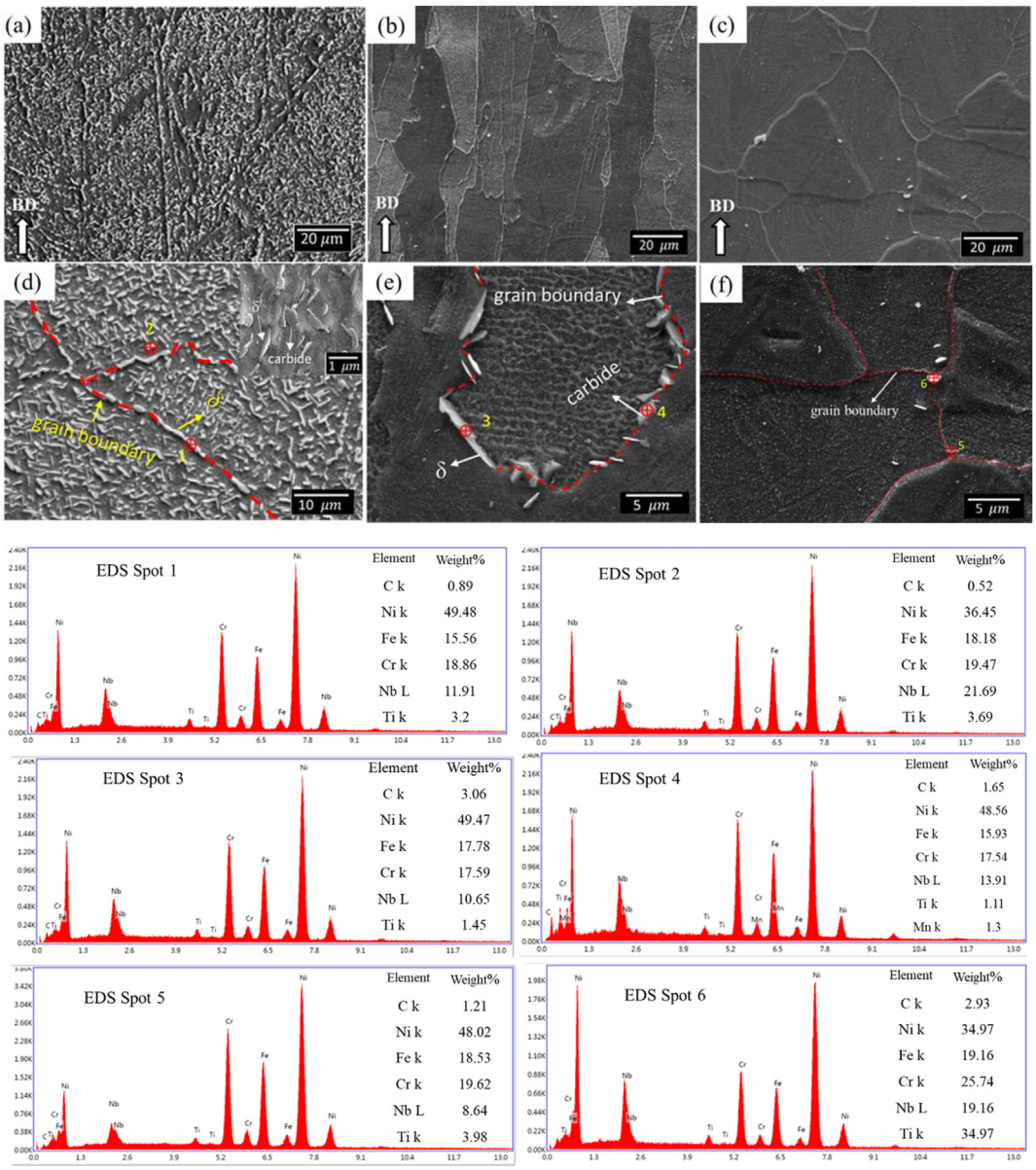

Fig. 4 – SEM images of (a, d) HT980, (b, e) HT1060, and (c, f) HT1130 samples at different magnifications. The EDS analysis corresponding to the spots 1–6 are presented.

Fig. 8 displays TEM analysis along with SAED patterns from the different components of the HT980 microstructure. The results reveal that the component marked in Fig. 8(a) is the acicular γ″ phase with (100)[001]γ//(100)[001]γ″ orientation relationship with γ matrix. However, the SAED patterns obtained from the particle in Fig. 8(e) indicated the existence of acicular δ phase with $(2\ \bar{2}0)[001]_{\gamma}//(001)[010]_{\delta}$ orientation relationship in the microstructure. Fig. 9(a) is the high-resolution TEM (HRTEM) image showing the ellipsoidal γ″ phase within γ grain in the HT980 sample. The Fast Fourier Transform (FFT) patterns corresponding to the marked particles (Fig. 10(b) and (c)) are consistent with the SAED patterns of Fig. 9(b) ($[001]_{\gamma}$) and Fig. 9(c) ($[100]_{\gamma''}$). The FFTs also prove the orientation relationship (100) $[001]_{\gamma''}$//(100) $[001]_{\gamma}$.

3.3. *Mechanical properties*

The effect of heat treatment on mechanical properties was investigated by performing stress rupture tests at 650 °C/750 MPa. The stress rupture results demonstrated in Fig. 10 and Table 3 reveal that the solution temperature considerably influences stress rupture performance of the LPBF fabricated IN718 superalloy. As can be seen, the most extended rupture life was related to the HT1060 sample with a failure time of about 78 h, while the HT980 specimen exhibited nearly one-third of the rupture life of the HT1060 specimen (about 30 h). In addition, the HT1130 sample with a rupture life around 52 h had better stress rupture behavior than the HT980 sample but exhibited a shorter rupture life than sample HT1060. The

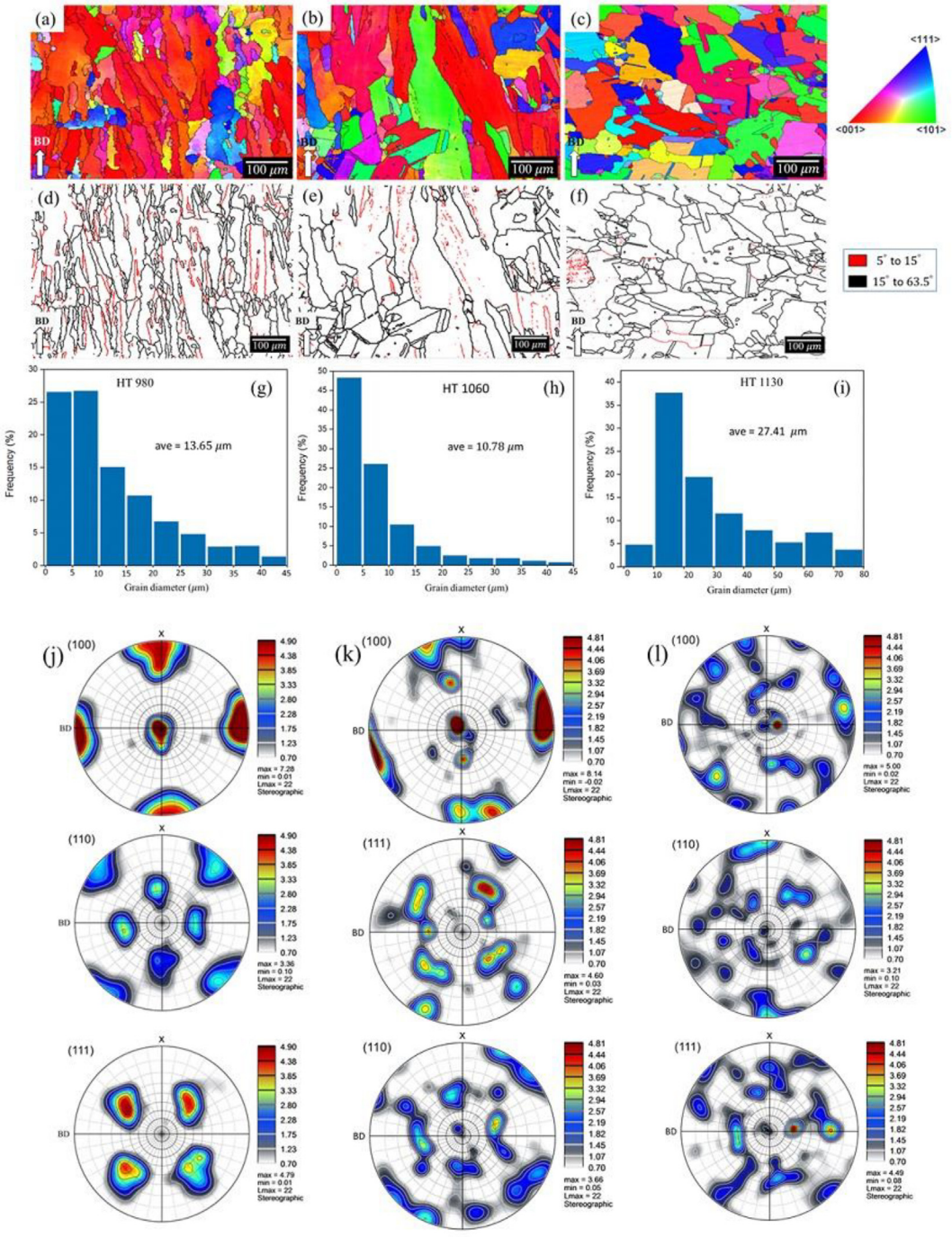

Fig. 5 – EBSD data of the (a, d, g, j) HT980, (b, e, h, k) HT1060, and (c, f, i, l) HT1130 alloys: (a, b, c) orientation maps, (d, e, f) grain boundary maps, (g, h, i) grain size distribution, and (j,k,l) pole figures.

creep rate–time curves for all three samples display a gradual decline in the primary stage. By entering the second creep step, the creep rate is minimized and stays almost steady, and with the onset of the third region, it accelerates until failure. The minimum creep rate in the second stage for the HT980 sample was also higher than other samples. The failure time of the samples in this research is consistent with the results obtained in the literature that were similar in testing and sampling conditions [25].

3.4. *Fractography*

In order to investigate fracture mechanism of the LPBF fabricated IN718 samples under different heat treatment conditions, the samples were subjected to failure analysis after the stress rupture tests. The SEM micrographs of the crept specimens are shown in Fig. 11. Fig. 11(a) –11(c) illustrate the fracture surfaces of the crept specimens. The presence of micro-cracks and creep cavities, mainly in grain boundaries,

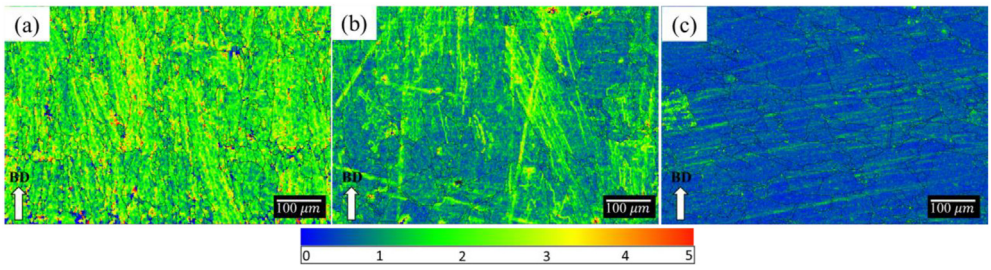

Fig. 6 – Kernel average misorientation maps of the (a) HT980, (b) HT1060 and (C) HT 1130 solution-treated samples.

reveals that the intergranular creep fracture has occurred in all specimens (micro-cracks and creep cavities are indicated by yellow arrows). As can be seen, wedge cracking (w-type) is formed on the triple point of grains in the HT980 sample (Fig. 11(a)). In addition, the fracture surface of the HT980 sample showed cleavage surface, which is an evidence of brittle fracture mode. However, on the fracture surface of the HT1060 sample (Fig. 11(b)), small shallow dimples can be seen next to the flat plates, while on the fracture surface of the HT980 sample, there were no traces of these dimples. Therefore, it can be said that a semi-brittle failure has been occurred in the HT1060 sample. The formation of very small dimple-like cavities in the failure surface of the HT1130 specimen (Fig. 11(c)) indicates that this specimen experienced ductile fracture during the stress rupture test. As revealed in Fig. 11(d) and (g), the micro-cracks are formed along grain boundaries around the δ or Laves phases in the HT980 specimen. In the HT1060 specimen, the formation and coalescence of creep cavities caused by grain boundaries sliding during the creep process have led to the creation of micro-cracks in the grain boundaries (Fig. 11(e) and (h)). The acicular δ phase is usually identified as an undesirable particle that has destructive effects on high-temperature mechanical properties. The incoherent interface between δ and γ matrix led to high interface energy, which may accelerate the nucleation of creep cavities. This can be the main factor in reducing the fracture time in the HT980 specimen. The fracture cross-section of the HT1130 sample is shown in Fig. 11(f) and (i), as well as the HT980 and HT1060 samples, display creep cavities and micro-cracks in the grain boundaries. Complete removal of δ phases and decrease of Laves particle from grain boundaries in the HT1130 specimen led to a decrease in creep cavities and micro-cracks and increased rupture life in this sample compared to the HT980 sample; nevertheless, its rupture life compared to the HT1060 specimen was dropped. This should be related to the effect of morphology and grain size on stress rupture properties which will be explained in the discussion section.

4. Discussion

4.1. *Grain morphologies and phase formation of the as-built specimen*

Microstructural observations revealed that a mixture of columnar and equiaxed grains was formed in the as-built specimen. The columnar grains resulted from the epitaxial grain growth which is occurred along the heat flow direction without an energy barrier, while the heterogeneous nucleation in areas with complex heat transmission, such as the overlapping areas or the areas near the solidification front, led to the formation of the equiaxed grains [26,27]. Characterization of the as-built sample also indicated that a cellular solidification structure was formed during the LPBF process. It is known that the ratio of temperature gradient (G) to solidification rate (R) determines the type of solidification structure [28]; the solidification structure becomes equiaxed grains at a lower G/R values, while cellular and finally planar by increasing this ratio [26,29]. Due to directional heat transfer and relatively high cooling rate in the LPBF process, the G/R has a moderate value; hence, the typical solidification structure in the LPBF samples is cellular [26,30]. It is observed from Fig. 3(b) that the cells grew at different orientations, which is the result of the random distribution of easy growth direction (the <100> direction in FCC metals) in the base plate [29].

As well-accepted, the main strengthening phase in the microstructure of IN718 is γ′′ (Ni_3Nb) precipitates, which affect mechanical properties, especially at high-temperature [31,32]. The element Nb has a critical role in controlling the formation of the γ′′ phase. However, Nb is easily segregated into the interdendritic regions during solidification, which leads to the formation of Laves phases in the intercellular area [33]. It can be said that the precipitates observed in the intercellular regions in Fig. 3(c) might be chain-like Laves phase, as already seen by many researchers in the LPBF fabricated IN718 alloy [5,34,35]. Laves is a hexagonally closed packed phase that contains a high amount of Niobium (Nb) and is generally undesirable in the γ even during annealing [36]. It should be noted that although the Laves phases are formed in the as-built specimen (as shown in Fig. 3(d)) and could remain in the microstructure of the solution-treated ones, it is possible to become undetectable by TEM due to the small regions under investigation.

4.2. *Impact of precipitation hardening treatment on grain morphology*

Fig. 5(d–f) show that fraction of the LAGBs has decreased from 34% in the as-built sample to 22% in the HT980, 19% in the HT1060, and 6% in the HT1130 samples. It is reported in literature that transformation of LAGBs to HAGBs during heat treatment can be proof of discontinuous static recrystallization (dSRX) [37], resulting in the formation of equiaxed grains

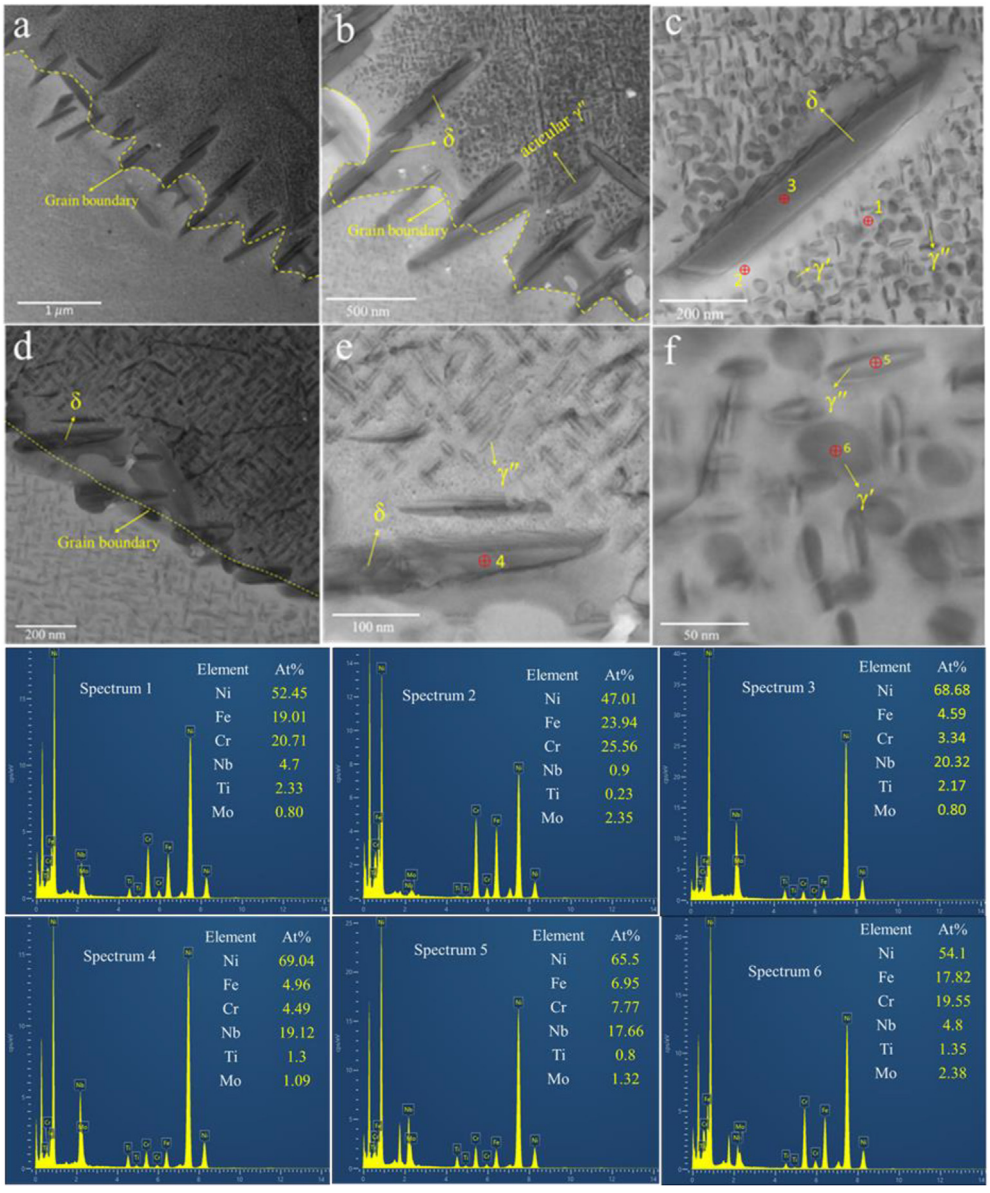

Fig. 7 – STEM images of with different heat treatments: (a, b, c) HT980, (d, e, f) HT1060, along with EDS analysis of the named points on the micrographs.

among the distorted columnar grains. Moreover, serrated boundaries, which can be seen in HT980 and HT1060 samples (Fig. 5(d and e)), are another indication of starting dSRX in low stacking fault energy (SFE) alloys such as IN718 [38]. Indeed, dSRX was started with nucleation of fine equiaxed grains at HAGBs of the HT980 and HT1060 samples. However, this transformation was not completed in these samples because of the low activation energy. The occurrence of dSRX transformation requires driving force as well as activation energy. The driving force of this transformation is generated during the rapid solidification in the LPBF process, and the activation energy should be provided from annealing temperature [39]. Presumably, the annealing temperature of 980 and 1060 °C for 1 h has not been sufficient to complete the recrystallization. On the contrary, enough activation energy is provided at 1130 °C, to complete dSRX in the HT1130 sample.

The main driving force for the nucleation of recrystallized grains is the residual stresses created during part fabrication in the LPBF process. Nevertheless, these residual stresses do not have a uniform distribution in the structure (as seen in KAM maps in Fig. 6) [37]. So, as can be seen in Fig. 5(a–c), some part of the microstructure is in the recrystallization stage, while in some areas where the amount of residual stresses is higher, they have already entered to grain growth stage. Hence, grain size is completely different after recrystallization in HT1130 sample (Fig. 5(c)).

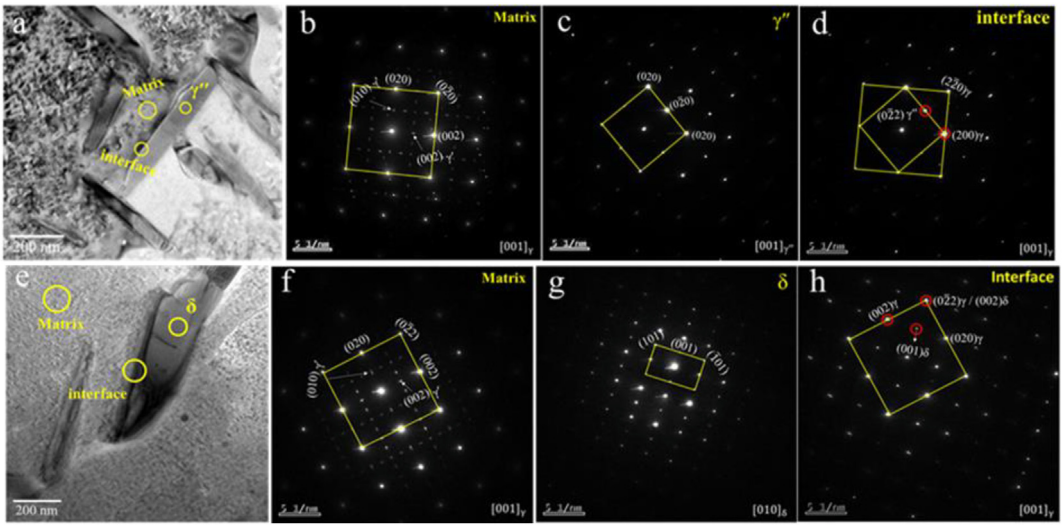

Fig. 8 – TEM BF images showing acicular phase in HT980 sample with their corresponding SAED patterns from precipitate, matrix, and their interface.

4.3. *Effect of precipitation hardening on second phase precipitation*

In the present study, the acicular δ phases were formed at both grain boundary and intragranular γ matrix in the HT980 sample (Fig. 4(a) and (d)) similar to the heat-treated IN718 alloy manufactured by LPBF process reported by many authors [24,40–42]. However, in the conventionally fabricated cast or wrought IN718 alloy, these phases are just precipitated at grain boundaries when sample heat treated. This issue is related to the existence of proper nucleation sites for precipitation inside the grains of the HT980 specimen due to the high density of dislocations which generated during the LPBF process. The high density of the LAGBs and distorted columnar grain boundaries are evidence of a high density of dislocations inside the grains. As shown in Fig. 5(d–f) in the HT980 sample, both features were more prominent than in the HT1060 and HT1130 samples. The results show that the occurrence of dSRX at high temperature (1130 °C used in this study) led to the annihilation of dislocation and could suppress the formation of the precipitates from inside the grains.

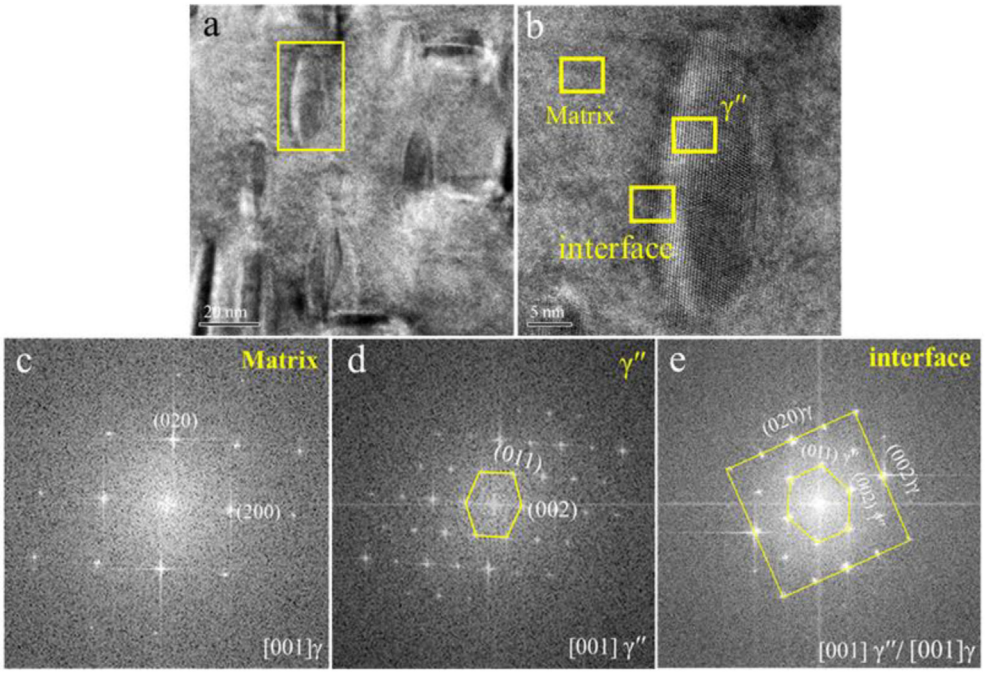

Fig. 9 – HRTEM images of the γ matrix showing ellipsoidal γ′′ phase. Corresponding FFTs of γ matrix, [001]-oriented γ′′, and interface of them.

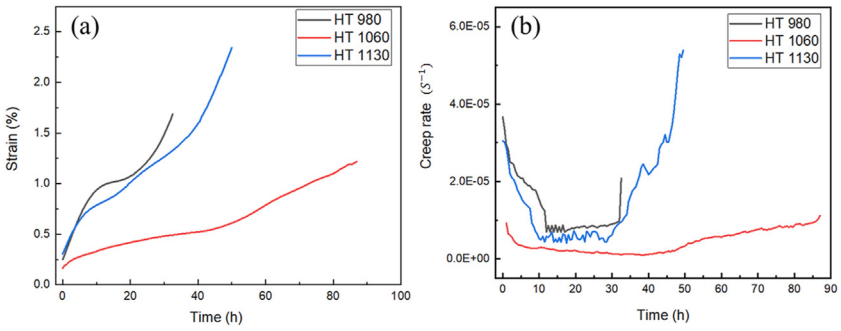

Fig. 10 – (a) Creep strain-time and (b) creep rate–time curves of the heat-treated samples with the constant stress of 650 MPa at 650 °C.

Characterization of the heat-treated samples indicated that the γ″ phases were formed by two distinct morphologies; the ellipsoidal γ″ precipitates with 20–80 nm in size within γ matrix, and coarser acicular γ″ precipitates along grain boundary (Fig. 7). The γ″ precipitates were also characterized with the same type by Cao et al. [23]. The SAED patterns (Fig. 8) confirms the presence of the [001] variants of γ″ along the [001] zone axis in the γ matrix. Precipitation of transgranular δ phases in the HT980 sample results in a decrease in the amount of available Nb in γ that is necessary to associate in the formation of γ″ particle [11,24]. However, since the solvus temperature of δ is around 1010 °C [11], annealing treatment above this temperature could dissolve the segregated elements into the γ matrix and provide more Nb for the formation of nano-scale γ″.

4.4. *Effect of precipitation hardening on stress rupture properties*

It is well-known that metal parts with larger grain sizes have better stress rupture properties than fine-grained alloys due to the fact that grain boundaries are the weak sites at high temperature conditions [43]. However, recent studies show that for the LPBF specimens, increasing grain size can be detrimental to both creep rupture time and creep strain rate until a certain point after which an increased grain size started to be beneficial [44]. In this study, the HT1060 specimen had smaller average grain size compared to other heat-treated samples while having a better rupture life. This shows that increasing the grain size does not necessarily improve creep performance of LPBFed IN718 samples. IN fact, a higher volume fraction of grain boundaries per unit area in the fine-grained materials could increase the nucleation potential of cracks. Nevertheless, recent studies indicate that when the predominant creep mechanism is intergranular failure, the finer grains could prevent grain boundary cracking [45,46]. It is observed in Fig. 10 that the intergranular fracture was the main creep mechanism in all three samples.

Table 3 – Stress-rupture test results of the heat-treated samples with the constant stress of 750 MPa at 650 °C.

Sample	Rupture life (hr)	Steady state rate (10^{-6} s^{-1})	Strain (%)
HT 980	30 ± 2	6.94 ± 0.27	1.69 ± 0.32
HT1060	78 ± 9	1.06 ± 0.02	1 ± 0.21
HT 1130	52 ± 3	4.82 ± 0.47	2.57 ± 0.22

Intergranular creep fracture mode mainly happens as a result of grain boundary sliding, which leads to the formation and coalescing of creep cavities near to second phase precipitates (principally δ phase) [13]. On the other hand, in the materials with a columnar grain structure, the cracks are more likely to propagate since their grain boundaries are flatter than those in the materials with equiaxed grains [47]. Therefore, the columnar grain boundaries containing δ phase in the HT980 specimen supply more chance for the nucleation and coalescing of creep cavities at grain boundaries and exhibit the shortest creep rupture life.

As already explained, residual stresses remain in the as-built parts due to the inherent characteristics of the LPBF process [11]. These residual stresses, which are the driving force for grain growth during heat treatment, are not distributed uniformly in the microstructure [37]. As a result, by entering the specimen into the grain growth stage (HT1130 in this study), inhomogeneous grain growth occurs, leading to the formation of a structure with non-uniform grain sizes. The presence of small regions of equiaxed grains besides large grains may act as nuclei of cracks and would be harmful for the stress rupture properties [48–50]. That is why the HT1130 sample exhibited a longer rupture life (52 h) compared to the HT980 one (30 h), but recorded a shorter rupture time than the sample HT1060 (78 h).

In addition, it is well known that the LPBF samples usually had a strong <100> texture along with building direction. It is found that this texture and grain orientation could lead to anisotropy in mechanical properties (such as yield strength), playing a role in reducing the creep life [44,51,52]. As mentioned in section 3.2, with increasing solution temperature this texture component became relatively weaker and as a result, led to an improved creep performance. On the other hand, the KAM results presented in Fig. 6 show that grain boundaries are the areas with a high misorientation, meaning the accumulation of dislocations. This stress concentration can also lead to increase the amount of precipitates on grain boundaries, which may accelerate the crack nucleation and

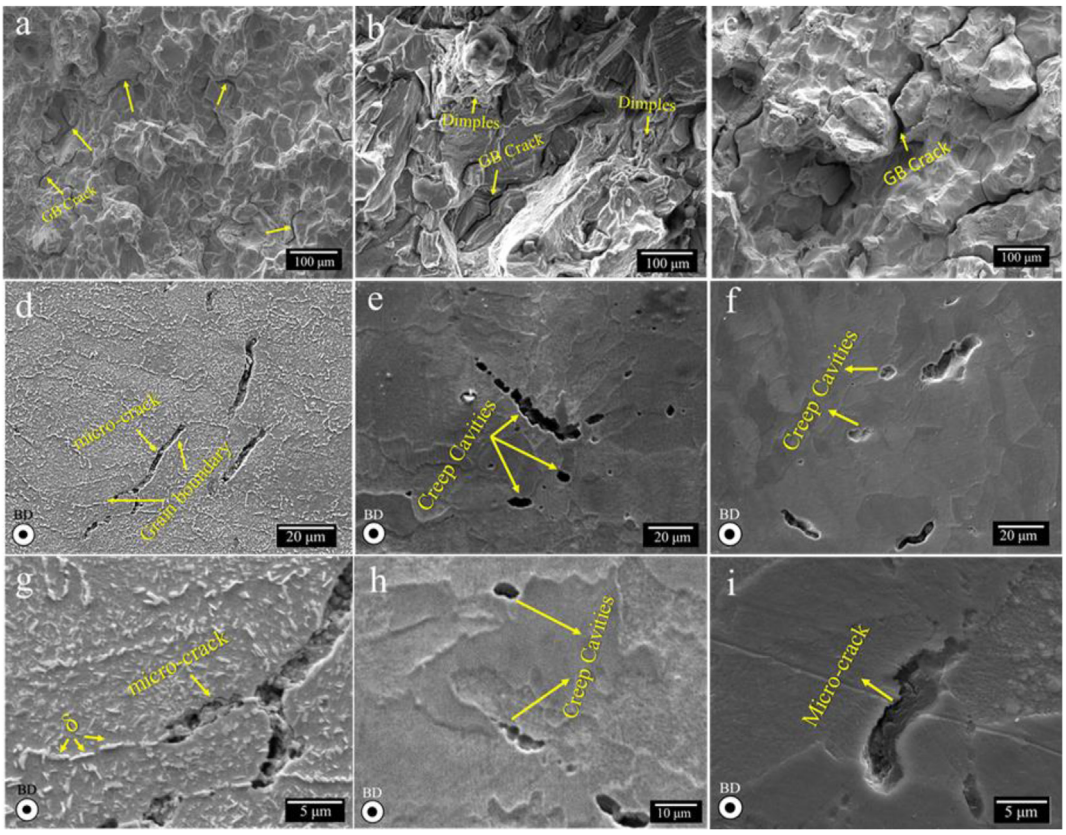

Fig. 11 – SEM images of the fracture surface of the crept samples of (a, d, g) HT980 (b, e, h) HT1060, and (C, f, i) HT1130.

creep voids formation at grain boundaries, resulting in a decreased rupture life.

Nevertheless, as mentioned before, the main strengthing phase in IN718 superalloy is γ″ precipitates which are contributed to the large lattice misfit with matrix. Precipitation of δ phase suppresses the formation of the γ″ phase by consuming Nb in the matrix. Thus, the γ″ volume fraction in the HT980 specimen may be lower than in the HT1060 and HT1130 samples. As reported in literature [13,16], with increasing solution temperature, the γ″ volume fraction could be increased, which led to improved high-temperature properties of the LPBFed IN718 sample. Besides, it was found that the average size of the nano-scale γ″ phase in the HT1060 sample (65.2 ± 22 nm) is larger than that those in the HT980 sample (33.6 ± 9.6 nm). In addition to fraction, the size of the strengthing γ″ phases also impacts stress rupture behavior of IN718 superalloy. It is therefore fair to say that the volume fraction and size of the γ″ precipitates in the HT1060 specimen were more than in the HT980 specimen, which may improve dislocation pinning of the particles and result in a longer fracture time for the HT1060 specimen. Moreover, precipitation of the δ phase along the grain boundaries because of their inherent brittleness could provide preferred sites for nucleation of creep cavities during a creep test [53]. As a consequence, dissolution of the δ phase along with enhancing the formation of γ″ phases, leads to elimination of the weak sites possessing potential to form creep cavities and micro-cracks.

5. Conclusions

In this study, stress rupture properties of the heat-treated LPBF fabricated IN718 samples with different solution temperatures were evaluated at 650 °C and 750 MPa. The implications of the microstructural features on stress rupture properties can be summarized as follows:

(1) Creep cavities and micro-cracks form along the grain boundaries around the δ or Laves phases, promoting intergranular fracture.
(2) The δ and Laves phases were dissolved in the matrix by the solution treatment at 1130 °C. However, stress rupture properties were not improved greatly due to inhomogeneous grain growth.
(3) A larger size and more uniform distribution of γ′/γ″ strengthening phases observed in the IN718 alloy solution treated at 1060 °C would result in a longer creep rupture life.

Declaration of Competing Interest

The authors declare that they have no known competing financial interests or personal relationships that could have appeared to influence the work reported in this paper.

REFERENCES

[1] Pollock TM, Tin S. Nickel-based superalloys for advanced turbine engines: chemistry, microstructure and properties. J Propul Power 2006;22:361–74.
[2] Akca E, Gursel A. A review on superalloys and IN718 nickel-based INCONEL superalloy. 2015. p. 3.
[3] Reed RC. The superalloys: fundamentals and applications. 1st ed. Cambridge university press; 2008.
[4] Sohrabi MJ, Mirzadeh H, Rafiei M. Revealing the as-cast and homogenized microstructures of niobium-bearing nickel-based superalloy. Int J 2019;13:320–30.
[5] Rezaei A, Rezaeian A, Kermanpur A, Badrossamay M, Foroozmehr E, Marashi M, et al. Materials Characterization Microstructural and mechanical anisotropy of selective laser melted IN718 superalloy at room and high temperatures using small punch test. Mater Char 2020;162:110200.
[6] Yang H, Meng L, Luo S, Wang Z. Microstructural evolution and mechanical performances of selective laser melting Inconel 718 from low to high laser power. J Alloys Compd 2020;828:154473.
[7] Moussaoui K, Rubio W, Mousseigne M, Sultan T, Rezai F. Effects of Selective Laser Melting additive manufacturing parameters of Inconel 718 on porosity, microstructure and mechanical properties. Mater Sci Eng, A 2018;735:182–90.
[8] Ni M, Liu S, Chen C, Li R, Zhang X, Zhou K. Effect of heat treatment on the microstructural evolution of a precipitation-hardened superalloy produced by selective laser melting. Mater Sci Eng, A 2019;748:275–85.
[9] Huang L, Cao Y, Zhang J, Gao X, Li G, Wang Y. Effect of heat treatment on the microstructure evolution and mechanical behaviour of a selective laser melted Inconel 718 alloy. J Alloys Compd 2021;865:158613.
[10] Cao M, Zhang D, Gao Y, Chen R, Huang G, Feng Z, et al. The effect of homogenization temperature on the microstructure and high temperature mechanical performance of SLM-fabricated IN718 alloy. Mater Sci Eng, A 2021;801:140427.
[11] Pröbstle M, Neumeier S, Hopfenmüller J, Freund LP, Niendorf T, Schwarze D, et al. Superior creep strength of a nickel-based superalloy produced by selective laser melting. Mater Sci Eng, A 2016;674:299–307. https://doi.org/10.1016/j.msea.2016.07.061.
[12] Kuo Y-L, Horikawa S, Kakehi K. Effects of build direction and heat treatment on creep properties of Ni-base superalloy built up by additive manufacturing. Scripta Mater 2017;129:74–8.
[13] Shi JJ, Li X, Zhang ZX, Cao GH, Russell AM, Zhou ZJ, et al. Study on the microstructure and creep behavior of Inconel 718 superalloy fabricated by selective laser melting. Mater Sci Eng, A 2019;765:1382.
[14] E139-11 A. Standard test methods for conducting creep, creep-rupture, and stress-rupture tests of metallic materials. Am Soc Test Mater Philadelphia, Pa 2011:19103.
[15] Zhang S, Lin X, Wang L, Yu X, Hu Y, Yang H, et al. Strengthening mechanisms in selective laser-melted Inconel718 superalloy. Mater Sci Eng, A 2021;812:141145.
[16] Shifeng W, Shuai L, Qingsong W, Yan C, Sheng Z, Yusheng S. Effect of molten pool boundaries on the mechanical properties of selective laser melting parts. J Mater Process Technol 2014;214:2660–7.
[17] Kumara C, Balachandramurthi AR, Goel S, Hanning F, Moverare J. Toward a better understanding of phase transformations in additive manufacturing of Alloy 718. Materialia 2020;13:100862.
[18] Huang W, Yang J, Yang H, Jing G, Wang Z, Zeng X. Heat treatment of Inconel 718 produced by selective laser melting: microstructure and mechanical properties. Mater Sci Eng, A 2019;750:98–107. https://doi.org/10.1016/j.msea.2019.02.046.
[19] Li J, Zhao Z, Bai P, Qu H, Liu B, Li L, et al. Microstructural evolution and mechanical properties of IN718 alloy fabricated by selective laser melting following different heat treatments. J Alloys Compd 2019;772:861–70.
[20] McLouth TD, Witkin DB, Lohser JR, Bean GE, Adams PM, Lingley ZR, et al. Influence of reduced carbon content on microstructure and mechanical behavior of Inconel 718 prepared by laser powder bed fusion. Addit Manuf Lett 2022;3:100037.
[21] Kong D, Dong C, Ni X, Zhang L, Yao J, Man C, et al. Mechanical properties and corrosion behavior of selective laser melted 316L stainless steel after different heat treatment processes. J Mater Sci Technol 2019;35:1499–507.
[22] Wright SI, Nowell MM, Field DP. A review of strain analysis using electron backscatter diffraction. Microsc Microanal 2011;17:316–29.
[23] Cao GH, Sun TY, Wang CH, Li X, Liu M, Zhang ZX, et al. Investigations of γ' γ'' and δ precipitates in heat-treated Inconel 718 alloy fabricated by selective laser melting. Mater Char 2018;136:398–406.
[24] Rezaei A, Kermanpur A, Rezaeian A, Badrossamay M, Foroozmehr E, Sadeghi F, et al. Contribution of hot isostatic pressing on densification, microstructure evolution, and mechanical anisotropy of additively manufactured IN718 Ni-based superalloy. Mater Sci Eng, A 2021:141721.
[25] Witkin DB, Hayes RW, McLouth TD, Bean GE. Anomalous notch rupture behavior of nickel-based superalloy inconel 718 due to fabrication by additive manufacturing. Metall Mater Trans A 2019;50:3458–65.
[26] DebRoy T, Wei HL, Zuback JS, Mukherjee T, Elmer JW, Milewski JO, et al. Additive manufacturing of metallic components-process, structure and properties. Prog Mater Sci 2018;92:112–224.
[27] Kok Y, Tan XP, Wang P, Nai MLS, Loh NH, Liu E, et al. Anisotropy and heterogeneity of microstructure and mechanical properties in metal additive manufacturing: a critical review. Mater Des 2018;139:565–86.
[28] Yadroitsev I, Yadroitsava I, Du Plessis A, MacDonald E. Fundamentals of laser powder bed fusion of metals. Elsevier; 2021.
[29] Kong D, Dong C, Wei S, Ni X, Zhang L, Li R, et al. About metastable cellular structure in additively manufactured austenitic stainless steels. Addit Manuf 2021;38:101804.
[30] Sander G, Tan J, Balan P, Gharbi O, Feenstra DR, Singer L, et al. Corrosion of additively manufactured alloys: a review. Corrosion 2018;74:1318–50.
[31] Hosseini E, Popovich VA. A review of mechanical properties of additively manufactured Inconel 718. Addit Manuf 2019;30:100877.
[32] Deng D, Peng RL, Brodin H, Moverare J. Microstructure and mechanical properties of Inconel 718 produced by selective laser melting: sample orientation dependence and effects of post heat treatments. Mater Sci Eng, A 2018;713:294–306.
[33] Popovich VA, Borisov EV, Popovich AA, Sufiiarov VS, Masaylo DV, Alzina L. Impact of heat treatment on mechanical behaviour of Inconel 718 processed with tailored microstructure by selective laser melting. Mater Des 2017;131:12–22.
[34] Wang LY, Zhou ZJ, Li CP, Chen GF, Zhang GP. Comparative investigation of small punch creep resistance of Inconel 718 fabricated by selective laser melting. Mater Sci Eng, A 2019;745:31–8.
[35] Du D, Dong A, Shu D, Zhu G, Sun B, Li X, et al. Influence of build orientation on microstructure, mechanical and corrosion behavior of Inconel 718 processed by selective laser melting 2019;760:469–80. https://doi.org/10.1016/j.msea.2019.05.013.

[36] Li X, Shi JJ, Wang CH, Cao GH, Russell AM, Zhou ZJ, et al. Effect of heat treatment on microstructure evolution of Inconel 718 alloy fabricated by selective laser melting. J Alloys Compd 2018;764:639–49.
[37] Cao Y, Bai P, Liu F, Hou X, Guo Y. Effect of the solution temperature on the precipitates and grain evolution of IN718 fabricated by laser additive manufacturing. Materials (Basel) 2020;13:340.
[38] Hadadzadeh A, Mokdad F, Wells MA, Chen DL. A new grain orientation spread approach to analyze the dynamic recrystallization behavior of a cast-homogenized Mg-Zn-Zr alloy using electron backscattered diffraction. Mater Sci Eng, A 2018;709:285–9.
[39] Mostafa A, Shahriari D, Rubio IP, Brailovski V, Jahazi M, Medraj M. Hot compression behavior and microstructure of selectively laser-melted IN718 alloy. Int J Adv Manuf Technol 2018;96:371–85.
[40] Trosch T, Strößner J, Völkl R, Glatzel U. Microstructure and mechanical properties of selective laser melted Inconel 718 compared to forging and casting. Mater Lett 2016;164:428–31.
[41] Farber B, Small KA, Allen C, Causton RJ, Nichols A, Simbolick J, et al. Correlation of mechanical properties to microstructure in Inconel 718 fabricated by direct metal laser sintering. Mater Sci Eng, A 2018;712:539–47.
[42] Gao Y, Zhang D, Cao M, Chen R, Feng Z, Poprawe R, et al. Effect of δ phase on high temperature mechanical performances of Inconel 718 fabricated with SLM process. Mater Sci Eng, A 2019;767:138327.
[43] Sherby OD, Burke PM. Mechanical behavior of crystalline solids at elevated temperature. Prog Mater Sci 1968;13:323–90.
[44] Sanchez S, Gaspard G, Hyde CJ, Ashcroft IA, Ravi GA, Clare AT. The creep behaviour of nickel alloy 718 manufactured by laser powder bed fusion. Mater Des 2021;204:109647.
[45] Xu Z, Murray JW, Hyde CJ, Clare AT. Effect of post processing on the creep performance of laser powder bed fused Inconel 718. Addit Manuf 2018;24:486–97.
[46] Badrossamay M, Rezaei A, Foroozmehr E, Maleki A, Foroozmehr A. Effects of increasing powder layer thickness on the microstructure, mechanical properties, and failure mechanism of IN718 superalloy fabricated by laser powder bed fusion. Int J Adv Manuf Technol 2022;118:1703–17.
[47] Xu Z, Cao L, Zhu Q, Guo C, Li X, Hu X. Materials Science & Engineering A Creep property of Inconel 718 superalloy produced by selective laser melting compared to forging. Mater Sci Eng, A 2020;794:139947.
[48] Cao J, Liu F, Lin X, Huang C, Chen J, Huang W. Effect of overlap rate on recrystallization behaviors of Laser Solid Formed Inconel 718 superalloy. Opt Laser Technol 2013;45:228–35.
[49] Kuo Y-L, Nagahari T, Kakehi K. The effect of post-processes on the microstructure and creep properties of alloy718 built up by selective laser melting. Materials (Basel) 2018;11:996.
[50] Kassner ME. Fundamentals of creep in metals and alloys. Butterworth-Heinemann; 2015.
[51] Zhang Y, Jing H, Xu L, Zhao L, Han Y, Liang J. Microstructure and texture study on an advanced heat-resistant alloy during creep. Mater Char 2017;130:156–72.
[52] Hsu S-E, Edwards GR, Sherby OD. Influence of texture on dislocation creep and grain boundary sliding in fine-grained cadmium. Acta Metall 1983;31:763–72.
[53] Oblak JM, Paulonis DF, Duvall DS. Coherency strengthening in Ni base alloys hardened by DO22 γ′ precipitates. Metall Mater Trans B 1974;5:143–53.